

# Critical and strong-coupling phases in one- and two-bath spin-boson models

Cheng Guo,<sup>1</sup> Andreas Weichselbaum,<sup>1</sup> Jan von Delft,<sup>1</sup> and Matthias Vojta<sup>2</sup>

<sup>1</sup>*Ludwig-Maximilians-Universität München, Germany*

<sup>2</sup>*Institut für Theoretische Physik, Technische Universität Dresden, 01062 Dresden, Germany*

(Dated: March 7, 2012)

For phase transitions in dissipative quantum impurity models, the existence of a quantum-to-classical correspondence has been discussed extensively. We introduce a variational matrix product state approach involving an optimized boson basis, rendering possible high-accuracy numerical studies across the entire phase diagram. For the sub-ohmic spin-boson model with a power-law bath spectrum  $\propto \omega^s$ , we confirm classical mean-field behavior for  $s < 1/2$ , correcting earlier numerical renormalization-group results. We also provide the first results for an XY-symmetric model of a spin coupled to two competing bosonic baths, where we find a rich phase diagram, including both critical and strong-coupling phases for  $s < 1$ , different from that of classical spin chains. This illustrates that symmetries are decisive for whether or not a quantum-to-classical correspondence exists.

Quantum spins in a bosonic environment are model systems in diverse areas of physics, ranging from dissipative quantum mechanics to impurities in magnets and biological systems [1]. In this paper we consider the spin-boson model and a generalization thereof to two baths, described by  $\mathcal{H}_{\text{sb}} = -\vec{h} \cdot \vec{\sigma}/2 + \mathcal{H}_{\text{bath}}$ , with

$$\mathcal{H}_{\text{bath}} = \sum_{i=x,y} \sum_q \left[ \omega_q \hat{B}_{qi}^\dagger \hat{B}_{qi} + \lambda_{qi} \frac{\sigma_i}{2} (\hat{B}_{qi} + \hat{B}_{qi}^\dagger) \right]. \quad (1)$$

The two-level system (or quantum spin, with  $\sigma_{x,y,z}$  being the vector of Pauli matrices) is coupled both to an external field  $\vec{h}$  and, via  $\sigma_x$  and  $\sigma_y$ , to two independent bosonic baths, whose spectral densities  $J_i(\omega) = \pi \sum_q \lambda_{qi}^2 \delta(\omega - \omega_q)$  are assumed to be of power-law form:

$$J_i(\omega) = 2\pi \alpha_i \omega_c^{1-s} \omega^s, \quad 0 < \omega < \omega_c = 1. \quad (2)$$

Such models are governed by the competition between the local field, which tends to point the spin in the  $\vec{h}$  direction, and the dissipative effects of the bosonic baths.

Indeed, the standard one-bath spin-boson model (SBM1), obtained for  $\alpha_y = h_y = 0$ , exhibits an interesting and much-studied [1–7] quantum phase transition (QPT) from a delocalized to a localized phase, with  $\langle \sigma_x \rangle = 0$  or  $\neq 0$ , respectively, as  $\alpha_x$  is increased past a critical coupling  $\alpha_{x,c}$ . According to statistical-mechanics arguments, this transition is in the same universality class as the thermal phase transition of the one-dimensional (1D) Ising model with  $1/r^{1+s}$  interactions. This quantum-to-classical correspondence (QCC) predicts mean-field exponents for  $s < 1/2$ , where the Ising model is above its upper-critical dimension [8, 9].

Checking this prediction numerically turned out to be challenging. Numerical renormalization-group (NRG) studies of SBM1 yielded non-mean-field exponents for  $s < 1/2$  [4], thereby seemingly negating the validity of the QCC. However, the authors of Ref. 4 subsequently concluded [10] that those results were not reliable, due to two inherent limitations of NRG, which they termed (i) Hilbert-space truncation and (ii) mass flow. Problem

(i) causes errors for critical exponents that characterize the flow into the localized phase at zero temperature, since  $\langle \sigma_x \rangle \neq 0$  induces shifts in the bosonic displacements  $\hat{X}_q = (\hat{B}_q + \hat{B}_q^\dagger)/\sqrt{2}$  of the bath oscillators which diverge in the low-energy limit for  $s < 1$  and hence cannot be adequately described in the truncated boson Hilbert space used by NRG [11]. Problem (ii) arises for non-zero temperatures, due to NRG's neglect of low-lying bath modes with energy smaller than temperature [12]. In contrast to NRG, two recent numerical studies of SBM1, using Monte Carlo methods [6] or a sparse polynomial basis [5], found mean-field exponents in agreement with the QCC. Nevertheless, other recent works continue to advocate the failure of the QCC [13].

The purpose of this Letter is twofold. First, we show how the problem (i) of Hilbert-space truncation can be controlled systematically by using a variational matrix product state (VMPS) approach formulated on a Wilson chain. The key idea is to variationally construct an optimized boson basis (OBB) that captures the bosonic shifts induced by  $\langle \sigma_x \rangle \neq 0$ . The VMPS results confirm the predictions of the QCC for the QPT of SBM1 at  $T = 0$ . (Problem (ii) is beyond the scope of this work.) Second, we use the VMPS approach to study an XY-symmetric version of the two-bath spin-boson model (SBM2), with  $\alpha_x = \alpha_y$ . This model arises, e.g., in the contexts of impurities in quantum magnets [14, 15] and of noisy qubits [14, 16], and displays the phenomenon of “frustration of decoherence” [14]: the two baths compete (rather than cooperate), each tending to localize a different component of the spin. As a result, a non-trivial intermediate-coupling (i.e. critical) phase has been proposed to emerge for  $s < 1$  [15], which has no classical analogue. To date, the existence of this phase could only be established in an expansion in  $(1 - s)$ , and no numerical results are available. Here we numerically investigate the phase diagram, and, surprisingly, find that the perturbative predictions are valid for a small range of  $s$  and  $\alpha$  only. We conclusively demonstrate the absence of a QCC for this model.

*Wilson chain.*— Following Refs. 3, 11, which adapted

Wilson's NRG to a bosonic bath, we discretize the latter using a logarithmic grid of frequencies  $\omega_{ki} \propto \Lambda^{-k}$  (with  $\Lambda > 1$  and  $k$  a positive integer) and map  $\mathcal{H}_{\text{bath}}$  onto a so-called Wilson chain of  $(L-1)$  bosonic sites:

$$\mathcal{H}_{\text{bath}}^{(L-1)} = \sum_{i=x,y} \left[ \sqrt{\frac{\eta_i}{\pi}} \frac{\sigma_i}{2} (\hat{b}_{1i} + \hat{b}_{1i}^\dagger) + \sum_{k=1}^{L-2} t_{ki} (\hat{b}_{ki}^\dagger \hat{b}_{k+1,i} + h.c.) + \epsilon_{ki} \hat{n}_{ki} \right]. \quad (3)$$

Here  $\hat{n}_{ki} = \hat{b}_{ki}^\dagger \hat{b}_{ki}$ , with eigenvalue  $n_{ki}$ , counts the bosons of type  $i$  on chain site  $k$ ; the detailed form of the hopping parameters  $t_{ki}$ , on-site energies  $\epsilon_{ki}$  (both  $\propto \Lambda^{-k}$ ), and the coupling  $\eta_i$  between spin component  $\sigma_i$  and site 1, are obtained following Refs. 17, 18. To render a numerical treatment feasible, the infinite-dimensional bosonic Hilbert space at each site  $k$  is truncated by restricting the boson number to  $0 \leq n_{ki} < d_k$  ( $d_k \leq 14$  in Refs. 3, 11).

The standard NRG strategy for finding the ground state of  $\mathcal{H}_{\text{sb}}^{(L)} = -\vec{h} \cdot \vec{\sigma}/2 + \mathcal{H}_{\text{bath}}^{(L-1)}$  is to iteratively diagonalize it one site at a time, keeping only the lowest-lying  $D$  energy eigenstates at each iteration. This yields a  $L$ -site matrix-product state (MPS) [19–21] of the following form (depicted in Fig. 1, dashed boxes):

$$|G\rangle = \sum_{\sigma=\uparrow,\downarrow} \sum_{\{\vec{n}\}} A^0[\sigma] A^1[n_1] \cdots A^{L-1}[n_{L-1}] |\sigma\rangle |\vec{n}\rangle. \quad (4)$$

Here  $|\sigma\rangle = |\uparrow\rangle, |\downarrow\rangle$  are eigenstates of  $\sigma_x$ ; the states  $|\vec{n}\rangle = |n_1, \dots, n_{L-1}\rangle$  form a basis of boson-number eigenstates within the truncated Fock space, with  $\hat{n}_{ki} |\vec{n}\rangle = n_{ki} |\vec{n}\rangle$  and  $0 \leq n_{ki} < d_k$ . For SBM2,  $n_k = (n_{kx}, n_{ky})$  labels the states of supersite  $k$  representing both chains. Each  $A^k[n_k]$  is a matrix (not necessarily square, but of maximal dimension  $D \times D$ , with  $A^0$  a row matrix and  $A^{L-1}$  a column matrix), with matrix elements  $(A^k[n_k])_{\alpha\beta}$ .

The need for Hilbert-space truncation with small  $d_k$  prevents NRG from accurately representing the shifts in the displacements  $\hat{x}_{ki} = (\hat{b}_{ki} + \hat{b}_{ki}^\dagger)/\sqrt{2}$  that occur in the localized phase. This problem can be avoided, in principle, by using an OBB, chosen such that it optimally represents the quantum fluctuations of *shifted* oscillators,  $\hat{x}'_{ki} = \hat{x}_{ki} - \langle \hat{x}_{ki} \rangle$ . While attempts to accommodate this strategy within standard NRG were unsuccessful [11], it was shown to work well [5] using an alternative representation of SBM1 using a sparse polynomial basis.

**VMPS method.**— We now show that an OBB can also be constructed on a Wilson chain. To this end, view the state  $|G\rangle$  of Eq. (4) as a MPS ansatz for the ground state of  $\mathcal{H}_{\text{sb}}^{(L)}$ , that is to be optimized *variationally* using standard MPS methods [19–21]. To allow the possibility of large bosonic shifts, we represent the  $A$ -matrix elements as [22–24] (Fig. 1, solid lines)

$$(A^k[n_k])_{\alpha\beta} = \sum_{\tilde{n}_k=0}^{d_{\text{opt}}-1} (\tilde{A}^k[\tilde{n}_k])_{\alpha\beta} V_{\tilde{n}_k n_k}^k \quad (k \geq 1). \quad (5)$$

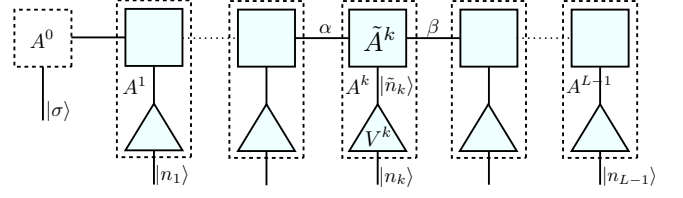


FIG. 1: Depiction of the MPS Eq. (4), with each  $A$ -matrix expressed in an optimal boson basis via  $A = \tilde{A}V$  [Eq. (5)].

Here  $V^k$  in effect implements a transformation to a new boson basis on site  $k$ , the OBB, of the form  $|\tilde{n}_k\rangle = \sum_{n_k=0}^{d_k-1} V_{\tilde{n}_k n_k}^k |n_k\rangle$  with  $0 \leq \tilde{n}_k < d_{\text{opt}}$ . (For SBM2,  $V^k$  is a rank-3 tensor.) This ansatz has the advantage that the size of the OBB,  $d_{\text{opt}}$ , can be chosen to be much smaller ( $d_{\text{opt}} \lesssim 50$ ) than  $d_k$ . Following standard DMRG strategy, we optimize the  $\tilde{A}^k$  and  $V^k$  matrices one site at a time through a series of variational sweeps through the Wilson chain. As further possible improvement before optimizing a given site, the requisite boson shift can be implemented by hand in the Hamiltonian itself: we first determine the “current” value of the bosonic shift  $\langle \hat{x}_{ki} \rangle$  using the current variational state  $|G\rangle$ , then use it as starting point to variationally optimize a new  $|G'\rangle$  with respect to the shifted Hamiltonian  $\mathcal{H}_{\text{sb}}'^{(L)}(\hat{b}_{ki}, \hat{b}_{ki}^\dagger) = \mathcal{H}_{\text{sb}}^{(L)}(\hat{b}'_{ki}, \hat{b}'_{ki}^\dagger)$ , with  $\hat{b}'_{ki} = \hat{b}_{ki} - \langle \hat{x}_{ki} \rangle/\sqrt{2}$ . The shifted OBB protocol, described in detail in Ref. 18, allows shifts that would have required  $d_k^{\text{eff}} \approx 10^{10}$  states in the original boson basis to be treated using rather small  $d_k$  (we used  $d_k = 100$ ).

**Spin-boson model.**— We applied the VMPS method to SBM1 ( $\alpha_y = h_y = 0$ ), with dissipation strength  $\alpha \equiv \alpha_x$  and fixed transverse field  $h_z = 0.1$ , at  $T = 0$ . We focussed on the QPT between the delocalized and localized phases in the subohmic case,  $s < 1$ . Here, the controversy [4–6, 10, 13] concerns the order-parameter exponents  $\beta$  and  $\delta$ , defined via  $\langle \sigma_x \rangle \propto (\alpha - \alpha_c)^\beta$  at  $h_x = 0$  and  $\langle \sigma_x \rangle \propto h_x^{1/\delta}$  at  $\alpha = \alpha_c$ , respectively. QCC predicts mean-field values  $\beta_{\text{MF}} = 1/2$ ,  $\delta_{\text{MF}} = 3$  for  $s < 1/2$  [8], whereas initial NRG results [4] showed  $s$ -dependent non-mean-field exponents.

In Fig. 2a, we show sample VMPS results for  $\langle \sigma_x \rangle$  vs.  $(\alpha - \alpha_c)$  for  $s = 0.3$  at  $h_x = 0$ , where  $\alpha_c$  was tuned to yield the best straight line on a log-log plot. The results display power-law behavior over more than 3 decades, with an exponent  $\beta = 0.50 \pm 0.03$ . Deviations at small  $(\alpha - \alpha_c)$  can be attributed to a combination of finite chain length and numerical errors of VMPS. Fig. 2b shows  $\langle \sigma_x \rangle$  vs.  $h_x$  at  $\alpha = \alpha_c$ , and a power-law fit over 6 decades results in  $\delta = 2.9 \pm 0.2$ . Power laws of similar quality can be obtained for all  $s \gtrsim 0.2$  [18, 25] (see [18], Fig. S7).

The exponents  $\beta$  and  $\delta$  obtained from such fits are summarized in Figs. 2c,d. For  $s < 1/2$  they are consistent with the mean-field values predicted by QCC, also found in Monte-Carlo [6] and exact-diagonalization studies [5], but are at variance with the NRG data of

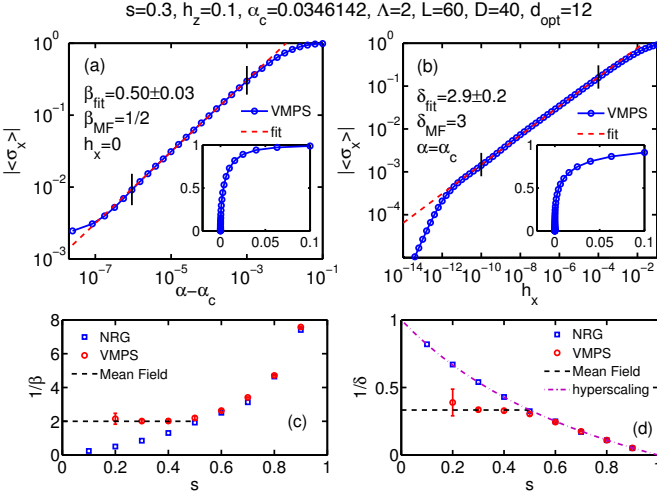


FIG. 2: VMPS results for the order parameter of SBM1 near criticality. a)  $\langle \sigma_x \rangle$  vs.  $(\alpha - \alpha_c)$  at  $h_x = 0$ , and b)  $\langle \sigma_x \rangle$  vs.  $h_x$  at  $\alpha = \alpha_c$ , on linear plots (insets) or log-log plots (main panels). Dashed lines are power-law fits in the ranges between the vertical marks. c, d) Comparison of the exponents  $\beta$  and  $\delta$  for different  $s$  obtained from VMPS, NRG [4], mean-field theory, and, in d), the exact hyperscaling result  $\delta = (1+s)/(1-s)$  which applies for  $s > 1/2$ . (See also [18], Fig. S7).

Ref. 4. Since both NRG and VMPS handle the same microscopic model  $\mathcal{H}_{\text{sb}}^{(L)}$  defined on the Wilson chain, but VMPS can deal with much larger  $d_k^{\text{eff}}$  values ( $\lesssim 10^{10}$  in Fig. 2) than NRG, the incorrect NRG results must originate from Hilbert-space truncation, as anticipated in Ref. 10. Indeed, artificially restricting  $d_k$  to small values in VMPS reproduces the incorrect NRG exponents (see [18], Fig. S6).

*Two-bath model.* — We now turn to SBM2, a generalization of the spin-boson model. Here, the two baths may represent distinct noise sources [14, 16] or XY-symmetric magnetic fluctuations [14, 15, 26]. Perturbation theory shows that the two baths compete: A straightforward expansion around the free-spin fixed point ( $\alpha = h = 0$ ) results in the following one-loop renormalization-group (RG) equations at  $\vec{h} = 0$ :

$$\beta(\alpha_x) = (1-s)\alpha_x - \alpha_x\alpha_y, \quad \beta(\alpha_y) = (1-s)\alpha_y - \alpha_x\alpha_y. \quad (6)$$

For  $\alpha \equiv \alpha_x = \alpha_y$ , these equations predict a stable intermediate-coupling fixed point at  $\alpha^* = 1 - s$ , describing a *critical* phase. It is characterized by  $\langle \vec{\sigma} \rangle = 0$ , a *non-linear* response of  $\langle \vec{\sigma} \rangle$  to an applied field  $\vec{h}$ , and a finite ground-state entropy smaller than  $\ln 2$ , all corresponding to a fluctuating fractional spin [15, 27]. This phase is unstable w.r.t. finite bath asymmetry ( $\alpha_x \neq \alpha_y$ ) and finite field. It had been assumed [15] that this critical phase exists for all  $0 < s < 1$  and is reached for any  $\alpha$ .

We have extensively studied SBM2 using VMPS; the results are summarized in the  $\vec{h} = 0$  phase diagram in Fig. 3a and the flow diagrams in Fig. 4. Most impor-

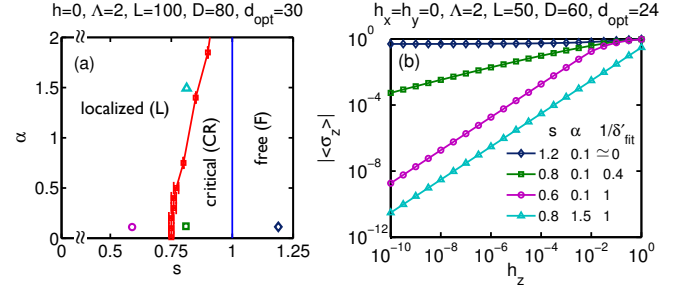


FIG. 3: a) Phase diagram of SBM2 in the  $s$ - $\alpha$  plane for  $\vec{h} = 0$ , with dissipation strength  $\alpha \equiv \alpha_x = \alpha_y$ . The critical phase only exists for  $s^* < s < 1$ , and its boundary  $\alpha_c \rightarrow \infty$  for  $s \rightarrow 1^-$ . (Ref. 18 describes the determination of the phase boundary and gives a 3D sketch of the  $s$ - $\alpha$ - $h_z$  phase diagram, see Fig. S8.) b) Transverse-field response of SBM2,  $\langle \sigma_z \rangle \propto h_z^{1/\delta'}$ , for four choices of  $s$  and  $\alpha$ , showing free (diamonds), critical (squares) and localized (triangles, circles) behavior.

tantly, we find that the critical phase (CR) indeed exists, but only for  $s^* < s < 1$ , with a universal  $s^* = 0.75 \pm 0.01$ . Even in this  $s$  range, the critical phase is left once  $\alpha$  is increased beyond a critical value  $\alpha_c(s)$ , which marks the location of a continuous QPT into a localized phase (L) with spontaneously broken XY symmetry and finite  $\langle \sigma_{x,y} \rangle$ . This localized phase exists down to  $s = 0$ , Fig. 3a. It can be destabilized by applying a transverse field  $h_z$  beyond a critical value  $h_z^c(\alpha)$ , marking the location of a continuous QPT into a delocalized phase (D) with unique ground state (see Ref. [18], Fig. S9). Finally, for  $s \geq 1$  we only find weak-coupling behavior, i.e., the impurity behaves as a free spin (F).

In Fig. 3b (and Ref. [18], Fig. S10) we show results for the transverse-field response,  $\langle \sigma_z \rangle \propto h_z^{1/\delta'}$ , which can be used to characterize the different zero-field phases.  $\langle \sigma_z \rangle$  is linear in  $h_z$  in L ( $\delta' = 1$ ), sublinear in CR ( $\delta' > 1$ ), and extrapolates to a finite value in F. For CR, a perturbative calculation gives  $1/\delta' = (1-s) + \mathcal{O}[(1-s)^2]$

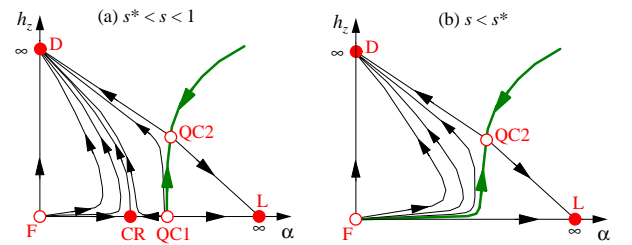


FIG. 4: Schematic RG flow for SBM2 in the  $\alpha$ - $h_z$  plane ( $h_x = h_y = 0$ ). The thick lines correspond to continuous QPT; the full (open) circles are stable (unstable) fixed points, for labels see text. a)  $s^* < s < 1$ : CR is reached for small  $\alpha$  and  $h_z = 0$ , it is separated from L by a QPT controlled by the multicritical QC1 fixed point. Eq. (6) implies that CR is located at  $\alpha^* = 1 - s + \mathcal{O}[(1-s)^2]$ . For finite  $h_z$ , a QPT between D and L occurs, controlled by QC2. b)  $0 < s < s^*$ : both CR and QC1 have disappeared, such that the only transition is between D and L.

[15] (confirmed numerically in Ref. [18], Fig. S11b), while the linear response in L corresponds to that of an ordered XY magnet to a field perpendicular to the easy plane.

From the VMPS results, we can schematically construct the RG flow, Fig. 4. There are three stable RG fixed points for  $s^* < s < 1$ , corresponding to the L, D, and CR phases. From this we deduce the existence of two unstable critical fixed points, QC1 and QC2, controlling the QPTs (Fig. 4a). Eq. (6) predicts that, as  $s \rightarrow 1^-$ , CR merges with F; this is consistent with our results for  $\delta'$  which indicate  $\delta' \rightarrow \infty$  as  $s \rightarrow 1^-$  (Ref. 18, Fig. S11b). The behavior of the phase boundary  $\alpha_c$  in Fig. 3a suggests that QC1 moves towards  $\alpha = \infty$  for  $s \rightarrow 1^-$ . Thus, for  $s \geq 1$  only F is stable on the  $\vec{h} = 0$  axis. Conversely, from Eq. (6) and Fig. 3a we extract that, upon lowering  $s$ , CR (QC1) moves to larger (smaller)  $\alpha$ . From the absence of CR for small  $s$  we then conclude that CR and QC1 merge and disappear as  $s \rightarrow s^{*+}$ . Consequently, for  $s < s^*$  we have only D and L as stable phases, separated by a transition controlled by QC2, Fig. 4b. The merger of CR and QC1 at  $s = s^*$  also implies that the phase boundary between CR and L in Fig. 3b at  $s^*$  is vertical at small  $\alpha$  (Ref. [18], Sec. V.C), because the merging point on the  $\alpha$  axis defines the finite value of  $\alpha_c$  at  $s \rightarrow s^{*+}$ .

Taken together, the physics of SBM2 is much richer than that of a classical XY-symmetric spin chain with long-range interactions, which only shows a single thermal phase transition [28]. Given this apparent failure of QCC for SBM2, it is useful to recall the arguments for QCC for SBM1: A Feynman path integral representation of Eq. (1), with non-zero  $h_z$ , can be written down using eigenstates of both  $\sigma_x$  and  $\sigma_z$ . Integrating out the bath generates a long-range (in time) interaction for  $\sigma_x$ . Subsequently, the  $\sigma_z$  degrees of freedom can be integrated out as well, leaving a model formulated in  $\sigma_x$  only. Re-interpreting the  $\sigma_x$  values for the individual time slices in terms of Ising spins, one arrives at a 1D Ising chain with both short-range and  $1/r^{1+s}$  interactions, with the thermodynamic limit corresponding to the  $T \rightarrow 0$  limit of the quantum model. Repeating this procedure for SBM2 with  $\vec{h} = 0$ , one obtains a Feynman path integral in terms of eigenstates of  $\sigma_x$  and  $\sigma_y$ . Importantly, both experience long-range interactions and hence neither can be integrated out. This leads to a representation in terms of *two* coupled Ising chains. However, upon re-exponentiating the matrix elements, the coupling between the two chains turns out to be imaginary, such that a classical interpretation is *not* possible [29]. In other words, a Feynman path-integral representation of SBM2 leads to negative Boltzmann weights, i.e., a sign problem.

*Conclusion.* — Our implementation of OBB-VMPS on the Wilson chain brings the Hilbert-space truncation problem of the bosonic NRG under control and allows for efficient ground-state computations of bosonic impurity models. We have used this to verify the QCC in SBM1 and to determine the phase diagram of SBM2, which is

shown to violate QCC. This underlines that symmetries are decisive for whether or not a QCC exists. A detailed study of the QPTs of SBM2 is left for future work.

The results for SBM2 also show that the predictions from weak-coupling RG are *not* valid for all parameters and bath exponents, in contrast to expectations. This implies that studying a *three*-bath version of the spin-boson model, which is related to the physics of a magnetic impurity in a quantum-critical magnet [15, 27], is an interesting future subject.

We thank A. Alvermann, S. Florens, S. Kirchner, K. Ingersent, Q. Si, A. Schiller and T. Vojta for helpful discussions. This research was supported by the Deutsche Forschungsgemeinschaft through SFB/TR12, SFB631, FOR960, by the German-Israeli Foundation through G-1035-36.14, and the NSF through PHY05-51164.

- 
- [1] A. J. Leggett *et al.*, Rev. Mod. Phys. **59**, 1 (1987).
  - [2] S. K. Kehrein and A. Mielke, Phys. Rev. A **219**, 313 (1996).
  - [3] R. Bulla, N. Tong, and M. Vojta, Phys. Rev. Lett. **91**, 170601 (2003).
  - [4] M. Vojta, N. Tong, and R. Bulla, Phys. Rev. Lett. **94**, 070604 (2005).
  - [5] A. Alvermann and H. Fehske, Phys. Rev. Lett. **102**, 150601 (2009).
  - [6] A. Winter *et al.*, Phys. Rev. Lett. **102**, 030601 (2009).
  - [7] H. Wong and Z. Chen, Phys. Rev. B **77**, 174305 (2008).
  - [8] M. E. Fisher, S. K. Ma, and B. G. Nickel, Phys. Rev. Lett. **29**, 917 (1972).
  - [9] E. Luijten and H. W. J. Blöte, Phys. Rev. B **56**, 8945 (1997).
  - [10] M. Vojta, N. Tong, and R. Bulla, Phys. Rev. Lett. **102**, 249904(E) (2009).
  - [11] R. Bulla *et al.*, Phys. Rev. B **71**, 045122 (2005).
  - [12] M. Vojta *et al.*, Phys. Rev. B **81**, 075122 (2010).
  - [13] S. Kirchner, Q. Si, and K. Ingersent, Phys. Rev. Lett. **102**, 166405 (2009).
  - [14] A. H. Castro-Neto *et al.*, Phys. Rev. Lett. **91**, 096401 (2003); E. Novais *et al.*, Phys. Rev. B **72**, 014417 (2005).
  - [15] L. Zhu and Q. Si, Phys. Rev. B **66**, 024426 (2002); G. Zarand and E. Demler, Phys. Rev. B **66**, 024427 (2002).
  - [16] D. V. Khveshchenko, Phys. Rev. B **69**, 153311 (2004).
  - [17] R. Žitko and T. Pruschke, Phys. Rev. B **79**, 085106 (2009).
  - [18] See supplemental material in the appendix.
  - [19] A. Weichselbaum *et al.*, Phys. Rev. B **80**, 165117 (2009).
  - [20] H. Saberi, A. Weichselbaum, and J. von Delft, Phys. Rev. B **78**, 035124 (2008).
  - [21] U. Schollwöck, Ann. Phys. **326**, 96 (2010).
  - [22] C. Zhang, E. Jeckelmann, and S. R. White, Phys. Rev. Lett. **80**, 2661 (1998).
  - [23] A. Weiße *et al.*, Phys. Rev. B **62**, R747 (2000).
  - [24] Y. Nishiyama, Eur. Phys. J. B **12**, 547 (1999).
  - [25] For very small  $s$ , high-accuracy numerical calculations inside the localized phase become prohibitively expensive.
  - [26] S. Kirchner *et al.*, PNAS **102**, 18824 (2005).
  - [27] M. Vojta, C. Buragohain and S. Sachdev, Phys. Rev. B **61**, 15152 (2000).
  - [28] J. M. Kosterlitz, Phys. Rev. Lett. **37**, 1577 (1976).
  - [29] T. Vojta, private communication.



# Supplementary Information for “Critical and strong-coupling phases in one- and two-bath spin-boson models”

Cheng Guo,<sup>1</sup> Andreas Weichselbaum,<sup>1</sup> Jan von Delft,<sup>1</sup> and Matthias Vojta<sup>2</sup>

<sup>1</sup>Ludwig-Maximilians-Universität München, Germany

<sup>2</sup>Institut für Theoretische Physik, Technische Universität Dresden, 01062 Dresden, Germany

(Dated: March 7, 2012)

## I. DISCRETIZATION AND MAPPING TO THE WILSON CHAIN

The spin-boson model represents a prototypical quantum-impurity setup, with the bath consisting of non-interacting particles. As such it is amenable to the concept of energy scale separation present in the NRG<sup>1–3</sup>. For this, the quantum impurity Hamiltonian of the spin-boson model is mapped onto a so-called Wilson chain, which includes two steps: (i) coarse graining of the bath (logarithmic discretization), followed (ii) by a mapping onto a semi-infinite bosonic chain with the spin-impurity connected to its starting point.

The bath spectral function  $J_i(\omega)$  of each bosonic bath  $i$  is assumed to be non-zero in the interval  $\omega \in [0, \omega_c]$ , with  $\omega_c$  an upper cutoff frequency. The bath spectral function  $J_i(\omega)$  is discretized then in energy-space into intervals  $[\omega_{m+1}, \omega_m]$ , marked by the decreasing sequence  $\omega_m$  ( $m = 0, 1, \dots$ ) with  $\omega_0 = \omega_c$  and  $\lim_{m \rightarrow \infty} \omega_m = 0$ . Assuming two identical baths  $i \in \{x, y\}$  that couple to the Pauli matrices  $\sigma_i$  of the impurity, respectively, the discretized Hamiltonian has the form

$$\mathcal{H}_{\text{bath}} = \sum_{i=x,y} \sum_{m=0}^{\infty} [\xi_m \hat{B}_{mi}^\dagger \hat{B}_{mi} + \frac{\sigma_i}{2\sqrt{\pi}} \gamma_m (\hat{B}_{mi} + \hat{B}_{mi}^\dagger)], \quad (\text{S1})$$

Here  $\hat{B}_{mi}^\dagger$  ( $\hat{B}_{mi}$ ) is the creation (annihilation) operator, respectively, of a free boson with energy  $\xi_m$ , that is coupled to the impurity spin with strength  $\gamma_m$ . Moreover,

$$\xi_m = \frac{\int_{\omega_{m+1}}^{\omega_m} J(x) dx}{\int_{\omega_{m+1}}^{\omega_m} (J(x)/x) dx} \quad \gamma_m = \left( \int_{\omega_{m+1}}^{\omega_m} J(x) dx \right)^{1/2}. \quad (\text{S2})$$

We prefer a logarithmic discretization scheme over a linear or power-law discretization, since the study of critical behavior requires very small energy scales to be resolved. This would require too many chain sites for linear and even power-law discretization schemes. Moreover, logarithmic discretization is ideally suited to represent scale-invariant physics near a quantum phase transition, and it has the advantage that characteristic NRG information, such as the energy flow diagram used to analyze the fixed points of the system, can be extracted from our VMPS results, if desired. (This will be elaborated upon in a separate publication<sup>4</sup>.)

In this paper we use the improved logarithmic discretization recently proposed by Žitko and Pruschke<sup>5</sup>. As this achieves a more consistent description of the bath, it reduces discretization effects and hence allows to determine phase boundaries such as the critical coupling strength  $\alpha_c$  more accurately. Thus we choose the discretization intervals as

$$\omega_0^z = \omega_c, \quad \omega_m^z = \omega_c \Lambda^{1-m-z}, \quad (m = 1, 2, 3, \dots) \quad (\text{S3})$$

with  $\Lambda > 1$  Wilson’s logarithmic discretization parameter<sup>1</sup>, and  $z \in ]0, 1]$  an arbitrary shift<sup>6</sup>. By solving the differential equation in App. C of Ref. 5 analytically, we obtain the following explicit expressions for the parameters in Eq. (S2):

$$\xi_0^z = \left[ \frac{1 - \Lambda^{-z(1+s)}}{(1+s)\ln\Lambda} - z + 1 \right]^{\frac{1}{1+s}}, \quad \xi_m^z = \left[ \frac{\Lambda^{-(1+s)(m+z)} (\Lambda^{1+s} - 1)}{(1+s)\ln\Lambda} \right]^{\frac{1}{1+s}}, \quad (m = 1, 2, 3, \dots) \quad (\text{S4})$$

$$\gamma_0^z = \sqrt{\frac{2\pi\alpha}{1+s} (1 - \Lambda^{-z(1+s)})}, \quad \gamma_m^z = \sqrt{\frac{2\pi\alpha}{1+s} (\Lambda^{1+s} - 1) \Lambda^{-(m+z)(1+s)}} \quad (m = 1, 2, 3, \dots) \quad (\text{S5})$$

Having discretized the Hamiltonian, the mapping onto the Wilson chain is done numerically using standard Lanczos tridiagonalization. For the calculations in this paper, we use  $z = 1$ .

We find that, with the discretization scheme of Žitko and Pruschke,<sup>5</sup> the  $\Lambda$ -dependence of  $\alpha_c$  is much weaker than for the traditional discretization scheme<sup>1,3</sup>, i.e.,  $\alpha_c$  converges rapidly as  $\Lambda$  is decreased towards 1. Similar to standard NRG, critical exponents do not depend on  $\Lambda$ , as shown in Fig. S1 for the exponent  $\beta$ .

## II. OBB-VMPS OPTIMIZATION PROCEDURE

As discussed in the main paper, we use a MPS of the following general form:

$$|G\rangle = \sum_{\sigma=\uparrow,\downarrow} \sum_{\{\vec{n}\}} A^0[\sigma] A^1[n_1] \cdots A^{L-1}[n_{L-1}] |\sigma\rangle |\vec{n}\rangle. \quad (\text{S6})$$

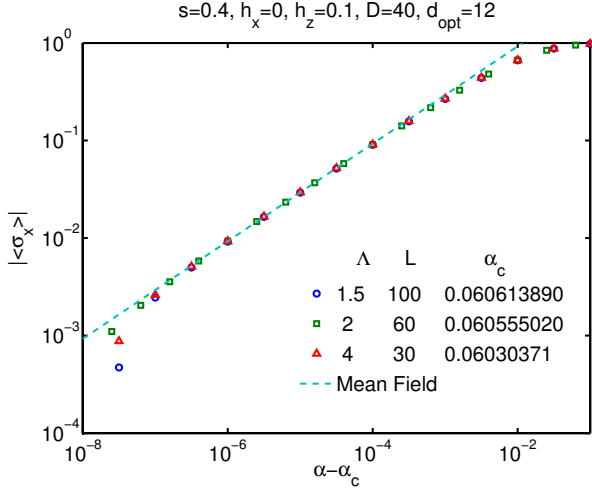


FIG. S1:  $\langle \sigma_x \rangle$  as function of  $(\alpha - \alpha_c)$  for SBM1, using three different choices of the discretization parameter  $\Lambda$  (and, correspondingly, different chain lengths  $L$ ). The data illustrate that the critical exponent  $\beta$ , obtained from power-law fits to this data, is essentially independent of  $\Lambda$ . The dashed line represents a power law  $\langle \sigma_x \rangle \propto (\alpha - \alpha_c)^\beta$  with mean-field exponent  $\beta_{\text{MF}} = 1/2$ .

The  $A$ -matrix elements are represented as

$$(A^k[n_k])_{\alpha\beta} = \sum_{\tilde{n}_k=0}^{d_{\text{opt}}-1} (\tilde{A}^k[\tilde{n}_k])_{\alpha\beta} V_{\tilde{n}_k n_k}^k \quad (k \geq 1), \quad (\text{S7})$$

in order to allow for the construction of an effective optimized boson basis (OBB) on each site  $k$ , given by

$$|\tilde{n}_k\rangle = \sum_{n_k=0}^{d_k-1} V_{\tilde{n}_k n_k}^k |n_k\rangle \quad (\tilde{n}_k = 0, \dots, d_{\text{opt}} - 1). \quad (\text{S8})$$

The VMPS ansatz (S6) for the ground state of the Wilson chain is completely analogous to standard finite-size DMRG<sup>7</sup>, and the use of an optimized local basis [Eqs. (S7) and (S8)] was pioneered in Ref. 8, finding subsequent applications in, for example, Refs. 9,10. The variational optimization of the resulting MPS with respect to the Hamiltonian  $\mathcal{H}_{\text{sb}}^{(L)}$  given in the main paper, depicted in Fig. 1 there, proceeds by iteratively updating the  $\tilde{A}$ - and  $V$ -matrices through a series of sweeps through the chain. Given the directed structure of the Wilson chain from large energy scales (left side of the MPS) to small energy scales (right side of the MPS), similar to the NRG, variational energy-lowering updates are performed only when sweeping from left to right. In contrast, during the reverse sweep from right to left the physical state (and its energy expectation value) is left unchanged. Nevertheless, during the reverse sweep the  $A$ -matrices are recast into a right-orthonormalized form, to ensure that the right low-energy part of the Wilson chain is described in terms of properly orthonormalized *effective* basis sets.

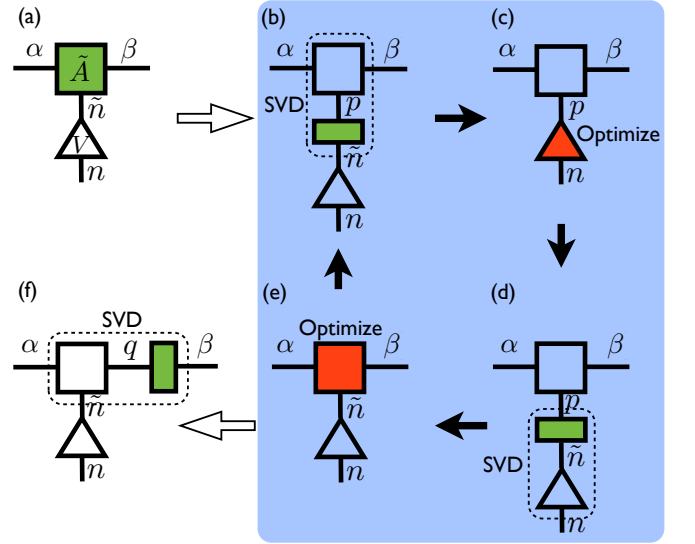


FIG. S2: Update procedure at one site when sweeping from left to right. The matrices surrounded by the dashed lines are the outcome of singular value decomposition (SVD). The filled squares or triangles indicate the “current focus” of each step. Filled arrows indicate the local update loop (highlighted by the shaded area), open arrows indicate its entry and exit.

To get started, the MPS is always initialized randomly, followed by proper orthonormalization. To update the coefficient spaces related to a given site  $k$  of the Wilson chain, we perform the following steps, depicted schematically in Fig. S2 (we suppress the index  $k$  below):

- (a) At a given site, the starting point is a well-defined local setting in terms of orthonormal basis sets  $|\alpha\rangle$ ,  $|\beta\rangle$ , and  $|\tilde{n}\rangle$  of the  $A$ -tensor for an effective left, right, and full local state space, respectively, as depicted in Fig. S2(a). The current approximation to the overall ground-state wave function therefore has its focus on the  $\tilde{A}$ -tensor of site  $n$ , and, setting  $\tilde{A}_{\alpha\beta\tilde{n}} \equiv (\tilde{A}[\tilde{n}])_{\alpha\beta}$ , can be written as

$$|\psi\rangle \equiv \sum_{\alpha\beta\tilde{n}} \tilde{A}_{\alpha\beta\tilde{n}} |\alpha\rangle |\beta\rangle |\tilde{n}\rangle. \quad (\text{S9})$$

- (b) Downward-orthonormalization of  $\tilde{A}$ -tensor to move the focus to the  $V$ -matrix: combine the left state space  $\alpha$  with the right state space  $\beta$  into one index, and use the effective local state space  $\tilde{n}$  as another index. Then singular value decomposition (SVD) of the resulting matrix,

$$\tilde{A}_{\alpha\beta\tilde{n}} = \tilde{A}_{(\alpha\beta)\tilde{n}} = \sum_p \tilde{A}'_{(\alpha\beta)p} \lambda_p B_{p\tilde{n}}, \quad (\text{S10})$$

generates a new orthonormal tensor  $\tilde{A}'$  that describes a combined description of the product space  $(\alpha, \beta)$ , such that

$$\sum_{(\alpha\beta)} \tilde{A}'_{(\alpha\beta)p} \tilde{A}'_{(\alpha\beta)p'}^* = \delta_{pp'}. \quad (\text{S11})$$

The wave function can now be represented as

$$|\psi\rangle = \sum_{p\tilde{n}} \lambda_p B_{p\tilde{n}} |p\rangle |\tilde{n}\rangle. \quad (\text{S12})$$

This description of the rest of the system in terms of an orthonormal effective basis  $|p\rangle$  is used to represent operators that connect the rest of the system with the current local state space. Being orthonormal, it also makes the numerics simple and stable.

- (c) By contracting the remaining box  $B$  from the last step onto the  $V$ -matrix, this shifts the focus down to the  $\tilde{V}$ -matrix

$$\tilde{V}_{pn} = \sum_{\tilde{n}} \lambda_p B_{p\tilde{n}} V_{\tilde{n}n}, \quad (\text{S13})$$

which thus has been altered. Having shifted the focus, the ground state is now represented as

$$|\psi\rangle \equiv \sum_{p,n} \tilde{V}_{pn} |p\rangle |n\rangle, \quad (\text{S14})$$

where the  $\tilde{V}$ -matrices connect the orthonormal state spaces  $p$  and with the local boson space  $n$ . So far, the transformation of  $|\psi\rangle$  has been exact with Eq. (S14) describing the same state as Eq. (S9). Transform the Hamiltonian and operators into the basis  $|p\rangle|n\rangle$  and solve the eigenvalue problem

$$\sum_{(pn)} H_{(p'n')(pn)} \tilde{V}_{(pn)} = E_g \tilde{V}_{(p'n')}, \quad (\text{S15})$$

for the ground state of the system. Thus the resulting  $\tilde{V}$ -matrix represents the *updated* ground state via Eq. (S14).

- (d) Upward-orthonormalization of the  $\tilde{V}$ -matrix: the singular value decomposition of  $\tilde{V}$ ,

$$\tilde{V}_{np} = \sum_{\tilde{n}} V_{n\tilde{n}} s_{\tilde{n}} C_{\tilde{n}p}, \quad (\text{S16})$$

provides a new effective description of the local boson space, such that the transformation matrix  $V$  from the original boson basis to the OBB is orthogonal:

$$\sum_n V_{n\tilde{n}} V_{n\tilde{n}'}^* = \delta_{\tilde{n}\tilde{n}'}. \quad (\text{S17})$$

Note that the singular values  $s_{\tilde{n}}$  indicate the relative importance of the optimal boson bases. We will come back to this point at the end of this section. At this step the wave function is

$$|\psi\rangle = \sum_{\tilde{n}p} s_{\tilde{n}} C_{\tilde{n}p} |\tilde{n}\rangle |p\rangle. \quad (\text{S18})$$

- (e) By contracting the remaining box  $s_{\tilde{n}}C$  from the previous step onto the  $\tilde{A}'$ -matrix, similar with step (c), the focus can be shifted to the  $\tilde{A}$ -matrix again:

$$\tilde{A}_{\alpha\beta\tilde{n}} = \sum_p \tilde{A}'_{\alpha\beta p} s_{\tilde{n}} C_{\tilde{n}p}. \quad (\text{S19})$$

The wave function is thus reexpressed in the same form as Eq. (S12). Now transform the local operators to the OBB  $|\tilde{n}\rangle$  using  $V$ , and optimize the  $\tilde{A}_{\alpha\beta\tilde{n}}$  matrix in the same way as done using the traditional VMPS method.

- (f) Combine the left and local indices and perform a singular value decomposition of the  $\tilde{A}_{\alpha\beta\tilde{n}}$  matrix:

$$\tilde{A}_{\alpha\beta\tilde{n}} = \tilde{A}_{(\alpha\tilde{n})\beta} = \sum_q \tilde{A}_{(\alpha\tilde{n})q} r_q F_{q\beta}. \quad (\text{S20})$$

The resulting tensor  $\tilde{A}_{\alpha q\tilde{n}}$  is left orthogonal:

$$\sum_{\alpha\tilde{n}} \tilde{A}_{\alpha q\tilde{n}} \tilde{A}_{\alpha q'\tilde{n}}^* = \delta_{qq'}. \quad (\text{S21})$$

Contracting the remaining  $r_q F_{q\beta}$  to the  $\tilde{A}$  tensor on the right side completes the update of the current site.

The OBB method enables us to increase the number  $d_k$  of local states that can be kept in the original basis from a few dozen to  $d_k \lesssim 10^4$ . (In the next section we shall show that by implementing explicit oscillator shifts, the *effective* number of local boson states that are accounted for in the unshifted basis can be increased to more than  $10^{10}$ .)

The two adjustable VMPS parameters are the dimension  $D$  of the VMPS matrices (corresponding to the number of DMRG states kept) and the dimension  $d_{\text{opt}}$  of the optimal boson basis. To exemplify the influence of  $D$  and  $d_{\text{opt}}$  on physical quantities, Fig. S3 plots the magnetization  $\langle\sigma_x\rangle$  for SBM1 as a function of  $\alpha$  for different  $D$  and  $d_{\text{opt}}$ . Clearly,  $\alpha_c$  is already well converged throughout. In practice, we chose  $D$  and  $d_{\text{opt}}$  large enough to ensure that all singular values  $[s_{\tilde{n}}$  and  $r_q$  in Eqs. (S16) and (S20)] larger than  $10^{-5}$  were retained throughout the entire Wilson chain, except possibly at its very end. We will explain this in more detail in the next section, when discussing Fig. S7 below.

For SBM2 with two bosonic baths, on the other hand, the combination of two boson sites into one supersite requires numerical parameters such as  $D$  and  $d_{\text{opt}}$  to be set to larger values than for SBM1. Nevertheless, we find that the number of kept states needed to ensure an accuracy comparable to that of SBM1 is smaller than the  $D^2$  or  $d_{\text{opt}}^2$  that might have been naively expected from the fact that the local state space now has a direct product structure.

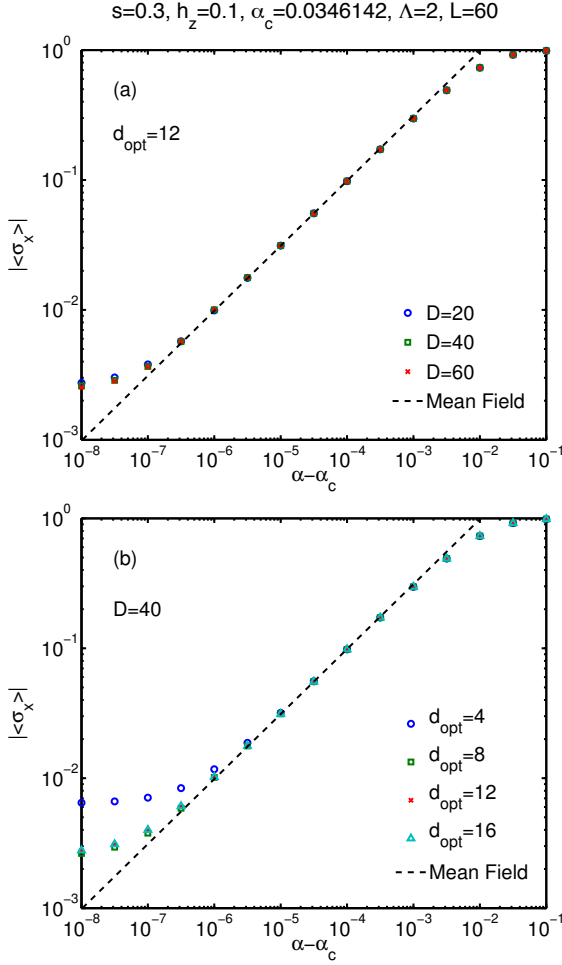


FIG. S3: Convergence check for the VMPS parameters  $D$  (a) and  $d_{\text{opt}}$  (b), for SBM1. The panels show  $\langle \sigma_x \rangle$  as function of  $\alpha_x$  for different choices of  $D$  and  $d_{\text{opt}}$ , respectively. Since critical exponents are obtained from fits to the linear parts of such curves, the resulting exponents are evidently not sensitive to  $D$  and  $d_{\text{opt}}$ . As in Fig. S1, the dashed lines show the mean-field power law with  $\beta_{\text{MF}} = 1/2$ .

### III. OBB WITH EXPLICIT SHIFTS

The OBB scheme described in the preceding section allows us to easily perform calculations on a desktop computer using local boson bases of dimension  $d_k \lesssim 10^4$ . This can be increased by at least 6 more orders of magnitude by analytically incorporating explicit shifts during the construction of OBB. The idea is to explicitly shift the harmonic oscillator coordinates  $\hat{x}_k$  by their equilibrium expectation values  $\langle \hat{x}_k \rangle$  (similar in spirit to the procedure used in Ref. 11), such that the OBB can be used to capture the quantum fluctuations of the shifted coordinate

$$\hat{x}'_k = \hat{x}_k - \langle \hat{x}_k \rangle. \quad (\text{S22})$$

We now describe explicitly how this is done.

We begin by noting that a shift corresponds to a uni-

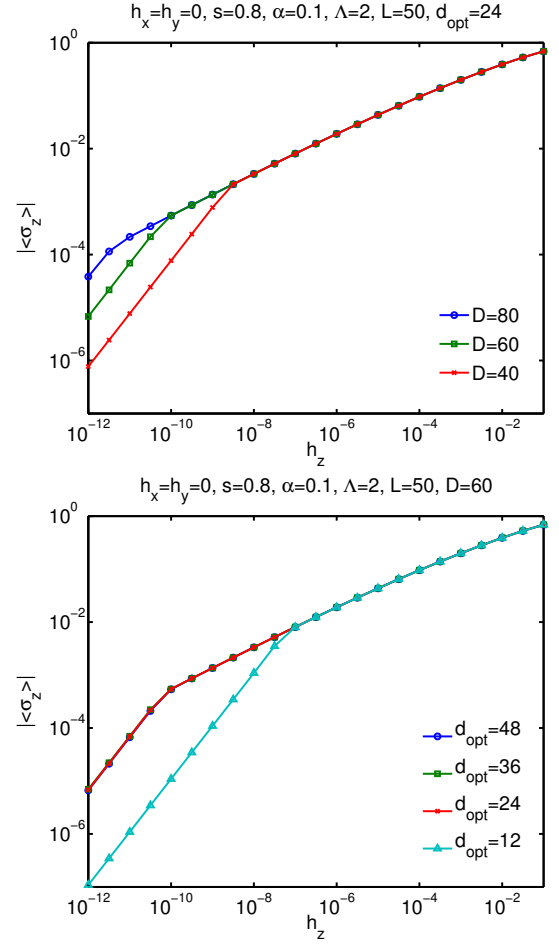


FIG. S4: Convergence check for the VMPS parameters  $D$  (a) and  $d_{\text{opt}}$  (b), for SBM2. The panels show the transverse-field response,  $|\langle \sigma_z \rangle|$  vs.  $h_z$  in the CR phase, with a robust sublinear power law. The deviations at smallest fields arise from small symmetry-breaking effects in the numerics which cause a linear response akin to an ordered state.

tary transformation

$$\hat{U}(\delta_k) = e^{\frac{\delta_k}{\sqrt{2}}(\hat{b}_k^\dagger - \hat{b}_k)} \quad (\text{S23})$$

such that,

$$\hat{b}'_k = \hat{U}^\dagger(\delta_k) \hat{b}_k \hat{U}(\delta_k) = \hat{b}_k + \frac{\delta_k}{\sqrt{2}} \quad (\text{S24})$$

on  $\hat{b}_k$  (similarly for  $\hat{b}_k^\dagger$ ). Thus the harmonic oscillator displacement  $\hat{x}_k \equiv \frac{1}{\sqrt{2}}(\hat{b}_k + \hat{b}_k^\dagger)$  is shifted to  $\hat{x}'_k = \hat{x}_k + \delta_k$ , and the local boson number operator to

$$\hat{n}'_k \equiv \hat{b}_k'^\dagger \hat{b}'_k = \hat{n}_k + \delta_k \hat{x}_k + \frac{\delta_k^2}{2}. \quad (\text{S25})$$

The shift can be implemented on the Hamiltonian level, by replacing the original Wilson-chain Hamiltonian by the shifted Hamiltonian

$$\mathcal{H}_{\text{sb}}'^{(L)}(\hat{b}_{ki}, \hat{b}_{ki}^\dagger) = \mathcal{H}_{\text{sb}}^{(L)}(\hat{b}'_{ki}, \hat{b}'_{ki}^\dagger). \quad (\text{S26})$$



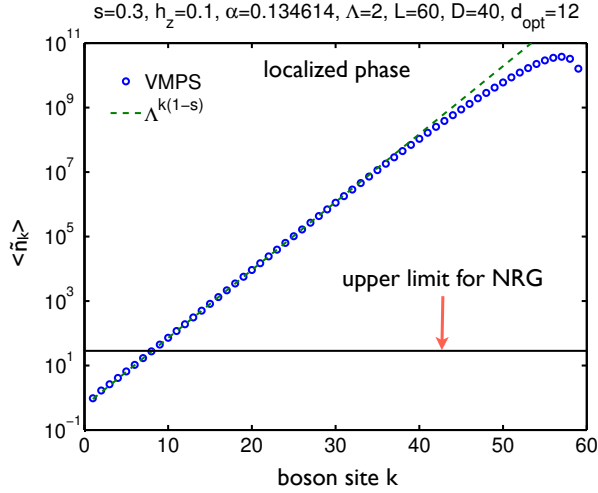


FIG. S5: Effective boson occupation number  $\langle \hat{n}_k \rangle$  in the original, unshifted Wilson-chain boson basis, as function of site index  $k$  along the Wilson chain, calculated for the localized phase of SBM1. Dashed line indicates the relation  $\langle \hat{n}_k \rangle \propto \Lambda^{k(1-s)}$  (see text). The finite size effect causes VMPS result deviate from this exponential relation at the end of the Wilson chain.

The local states  $|n_k\rangle$  in Eq. (S8) now represent Fock states of the shifted oscillators.

To incorporate explicit shifts within the OBB sweeping strategy described in the last section, we calculate the ground state expectation value  $\langle \hat{x}_k \rangle$  of the current site after step (e). We then set  $\delta_k = -\langle \hat{x}_k \rangle$  in Eqs. (S24) and (S25), thereby ensuring that the shifted coordinate  $\hat{x}'_k$  corresponds to Eq. (S22). We subsequently move back to step (b) and implement the shift in the Hamiltonian. (In practice, it is convenient to preserve the form of the Hamiltonian itself, and instead to change the matrix representation of the operators  $\hat{b}_k, \hat{b}_k^\dagger$  and  $\hat{n}_k$  to implement the shift of Eq. (24).) Then we repeat the local update loop of the sequence (b), (c), (d), (e) (Fig. S2) until the shift converges. Finally, we move to step (f) and the next site.

The SBB method allows us to reach boson shifts  $\langle \hat{x}_k \rangle$  so large that their description within the unshifted boson basis would require local dimensions of order  $d_k^{\text{eff}} \simeq 10^{10}$ , while nevertheless keeping the actual number of boson states in the *shifted* basis reasonably small, typically  $d_k \lesssim 10^2$ . A typical result for the resulting boson occupation numbers  $\langle \hat{n}_k \rangle$  in the original, unshifted Wilson-chain boson basis is shown in Fig. S5, calculated in the localized phase. Since the boson shifts for the bosons in the original definition of SBM1 scale as<sup>3</sup>  $\langle \hat{x}_k \rangle \simeq \omega_k^{(s-1)/2}$ , with  $\omega_k \propto \Lambda^{-k}$ , we expect and indeed find that  $\langle \hat{n}_k \rangle$  increases exponentially with  $k$ , as  $\Lambda^{k(1-s)}$ .

An accurate representation of this exponential rise, as achieved by our VMPS scheme, is essential for obtaining correct results for critical exponents. The detrimental effects of Hilbert space truncation are illustrated vividly in Fig. S6. It shows  $\langle \sigma_x \rangle$  vs.  $(\alpha - \alpha_c)$  for SBM1, calcu-

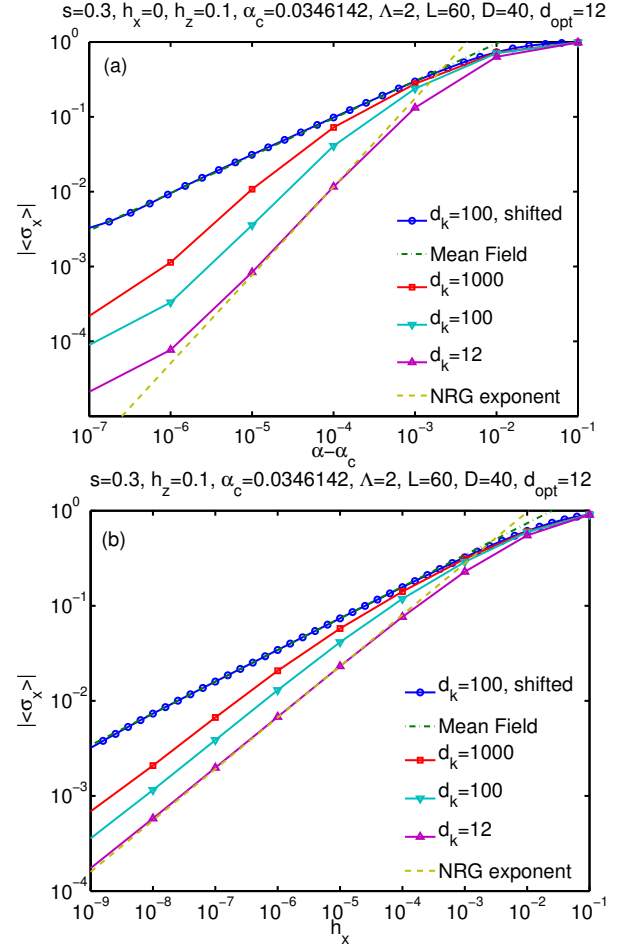


FIG. S6: The effect of Hilbert space truncation on the calculation of the SBM1 critical exponents  $\beta$  in (a) and  $\delta$  in (b). The calculation labeled “ $d_k = 100$ , shifted” was performed using the OBB method with explicit shifts, without setting any maximum value for the size of the shifts, i.e. without restricting  $d_k^{\text{eff}}$ . Dashed straight lines correspond to power laws with exponents  $\beta_{\text{NRG}} = 1.18$  and  $\delta_{\text{NRG}} = 1.85$  obtained by NRG<sup>13</sup>.  $\delta_{\text{NRG}}$  agrees with the hyperscaling exponent  $\delta = (1+s)/(1-s)$  that applies for  $s > 1/2$ , see Sec. IV C below.<sup>16</sup>

lated for several upper limits on the size  $d_k$  of the local boson basis. While the exponents obtained by NRG<sup>13</sup> (indicated by dashed lines) correspond to  $d_k \leq 12$ , the curves clearly change strongly as  $d_k$  is increased. Indeed, fully converged results are obtained only when the local boson basis can be taken to have “unlimited” size, as is the case for the explicit shifting strategy discussed above.

With the SBB method, the results for chain length  $L = 60$  shown in this paper can be obtained within a few hours on a desktop computer. Note, though, that in the localized phase the total time needed for the calculation increases exponentially with  $L$ . The reason is that the converged value for the effective shift  $\langle \hat{x}_k \rangle$  increases exponentially with  $k$  as

$$\langle \hat{x}_k \rangle \sim \Lambda^{k(1-s)/2}, \quad (\text{S27})$$

as explained above. However, the “sweeping step size” for  $\langle \hat{x}_k \rangle$ , i.e. the change in this quantity from one sweep to the next, is limited, in effect, by the dimension  $d_k$  of the shifted local boson basis. Consequently, the number of sweeps needed to achieve convergence for  $\langle \hat{x}_k \rangle$  increases exponentially with  $k$  (and making an informed initial guess for the requisite shift  $\langle \hat{x}_k \rangle$  does not really help in speeding up its accurate determination).

For a given set of convergence criteria, the exponential growth in the shifts  $\langle \hat{x}_k \rangle$  is accompanied by a similar growth in the absolute errors in their numerical determination. The consequences of this for SBM1 can be seen in Figs. S7(a) and S7(b), which show examples of the singular values  $r_q$  [Eq. (S20)] and  $s_{\tilde{n}}$  [Eq. (S16)], respectively, as functions of the Wilson chain  $k$ : when  $k$  becomes large, the lower end of the singular value shows an increasing amount of scatter. This implies that these singular values are not yet properly converged, which is directly correlated to the uncertainties in the oscillator shifts. Better convergence *can* be achieved by using stricter convergence criteria, as illustrated by Figs. S7(c) and S7(d), but only at a considerable increase in computation time, essentially using up to several hundreds of sweeps. We have thus adopted a compromise between accuracy and computation time: we chose  $D$ ,  $d_{\text{opt}}$  and the shift convergence criteria such that throughout the entire Wilson chain, all discarded singular values were smaller than  $10^{-5}$ , except possibly for an increase in this tolerance at the very end of the chain, of the type seen in Figs. S7(a) and S7(b). We have checked explicitly that not-optimally-converged shifts and singular values towards the end of the Wilson chain do not noticeably affect the resulting physical quantities of interest, i.e. that these are already well converged nevertheless.

Interestingly, we have found that for SBM2 it is easier to obtain a well-converged shift in the localized phase than for SBM1, because the competition between the two chains causes the increase in oscillator shifts near the end of the Wilson chain to be much smaller for SBM2 than SBM1, as illustrated in Fig. S8. Near the chain’s beginning, in contrast, the singular values for SBM2 were found to be bigger than for SBM1, but we nevertheless ensured throughout that only singular values below the  $10^{-5}$  tolerance were discarded.

#### IV. ADDITIONAL RESULTS FOR SBM1

##### A. Determination of phase boundary

We have explored a number of different methods for determining the phase boundary between the localized and delocalized phases, all of which yield essentially equivalent results. (Fortunately, no oscillator-shift-related convergence problems occur in this context, since the oscillator shifts are essentially zero at the phase boundary.)

1. “Best power law”. As mentioned in the main paper, our “standard method” for determining  $\alpha_c$  has been

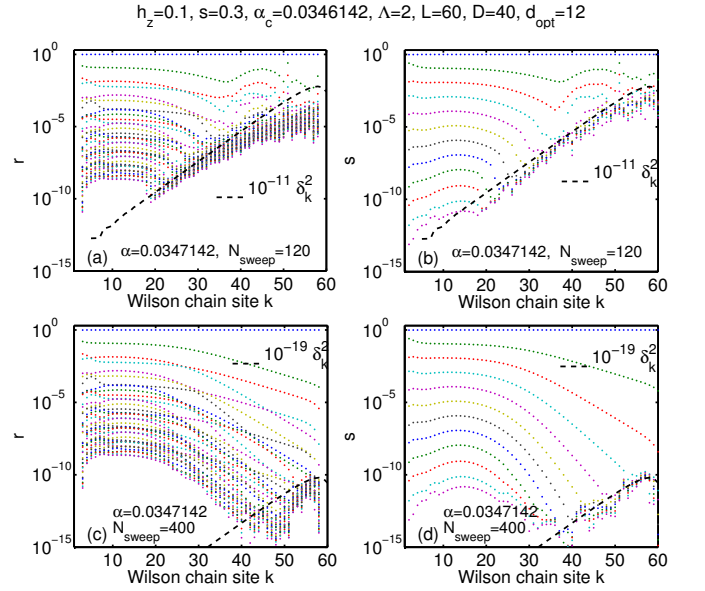


FIG. S7: Panels (a,c) and (b,d) show examples of the singular values  $r_q$  [Eq. (S20)] and  $s_{\tilde{n}}$  [Eq. (S16)], respectively, as functions of the Wilson chain  $k$ , calculated in the localized phase of SBM1. Panels (c,d) show the same quantities as (a,b), but calculated using stricter convergence criteria requiring more sweeps, resulting in better-converged singular values [see discussion after Eq. (S27)]. The maximum value of  $\langle \hat{n}_k \rangle$  in this example is of order  $10^8$ , corresponding to a maximum shift  $\langle \delta_k \rangle$  is of order  $10^4$ . The diagonal dashed lines show the  $k$ -dependence of the shifts  $\delta_k^2$ , multiplied by a constant prefactor that was chosen by hand in such a way that the dashed lines lie near the onset of noisiness at the lower end of the singular value spectra. This reveals the direct correlation between the exponential increase of  $\delta_k^2$ , which directly enters the Hamiltonian, and the noise in the smallest singular values.

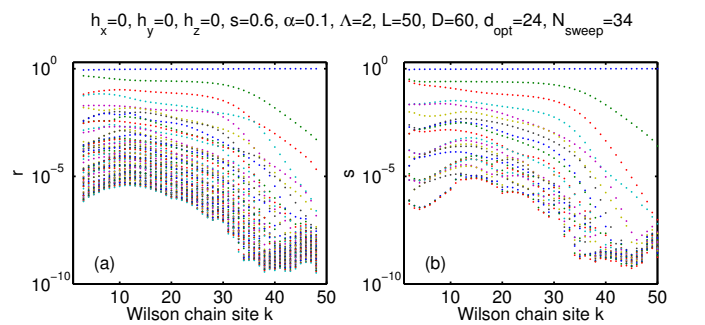


FIG. S8: Panels (a,b) show examples of the singular values  $r_q$  [Eq. (S20)] and  $s_{\tilde{n}}$  [Eq. (S16)], respectively, as functions of the Wilson chain  $k$ , calculated in the localized regime of SBM2. For all the SBM2 parameters studied in this paper, the maximum effective boson occupation number  $\langle \hat{n}_k \rangle$  is relatively much smaller than those we found in SBM1 ( $\langle \hat{n}_k \rangle < 10^5$ ), which results a faster convergence of shift  $\langle \delta_k \rangle$ . In this typical example for SBM2, we get converged singular values already with  $N_{\text{sweep}} = 34$ .

to tune it such that  $\langle \sigma_x \rangle$  vs.  $(\alpha_x - \alpha_c)$  yields the best straight line on a log-log plot. This turned out to be the most convenient way of getting accurate critical exponents.

**2. Energy flow diagrams.** In NRG, energy-flow diagrams<sup>1</sup> can be used to accurately determine the phase boundary of a quantum phase transition, since the degeneracies of low-lying levels typically differ for the two phases to be distinguished. It is possible to generate such energy-flow diagrams also within the VMPS approach<sup>12</sup>, by calculating the eigenstates of the left block's Hamiltonian at each site when sweeping from left (large energy scales) to right (small energy scales), and then appropriately rescaling and shifting the resulting eigenenergies<sup>1</sup>. Details of this procedure and explicit examples of flow diagrams obtained in this manner will be presented elsewhere<sup>4</sup>.

Energy-flow diagrams, however, are sensitive to relevant perturbations in terms of small numerical inaccuracies at large energies, i.e. early Wilson shells. This can lead to the artificial breaking of symmetries. For example, the Hamiltonian of SBM1 at  $h_x = 0$  commutes with the parity operator

$$\hat{P} \equiv \sigma_x e^{i\pi \hat{N}}, \quad (\text{S28})$$

where  $\hat{N} = \sum_k \hat{b}_k^\dagger \hat{b}_k$  counts the total number of bosons on the entire Wilson chain. The corresponding parity symmetry guarantees that the ground state is two-fold degenerate. However, this degeneracy is typically broken by numerical inaccuracies, unless the symmetry is explicitly implemented in the numerical code. We have done so, and flow-diagrams resulting from a parity-symmetric version of our code yield  $\alpha_c$  values in agreement with the “standard method” used in the main paper.

**3. Diverging boson number.** Another procedure for determining  $\alpha_c$  is to plot the boson occupation number for all sites of the Wilson chain: a divergence of  $\langle \hat{n}_k \rangle$  with Wilson-chain index  $k$ , as seen in Fig. S5, is a signature of the localized phase.

## B. Critical exponents

Fig. S9 shows some typical data sets used to extract the critical exponents  $\beta$  and  $\delta$  for  $s < 1$  shown in Figs. 1c,d of the main text. This allows to assess the accuracy of the VMPS method in the quantum critical regime.

To properly describe the critical behavior, the Wilson chain must be long enough to resolve energy scales down to the scale  $T_* \propto |\alpha - \alpha_c|^\nu$ , which bounds the quantum critical regime<sup>2</sup>; here  $\nu$  is the correlation-length exponent. Now, the lowest energy scale accessible for a bosonic Wilson chain of length  $L$ , i.e.  $L - 1$  boson sites, is  $\Lambda^{-L}$ . Thus, to determine  $\alpha_c$  with an accuracy of, say,  $10^{-a}$ , we need  $\Lambda^{-(L-1)} \lesssim T_* \propto 10^{-a\nu}$ , implying that the requisite chain length scales as

$$L \sim a\nu \frac{\ln(10)}{\ln \Lambda}. \quad (\text{S29})$$

For SBM1, the correlation-length exponent becomes large for small  $s$ , see Fig. 5a of Ref. 2, and hence the requisite chain length increases with decreasing  $s$ , too. Together with Eq. (S27), according to which the largest shifts at the end of the chain scale as  $\Lambda^{L(1-s)/2}$ , this implies that in the localized phase, the sweep time needed to reach convergence increases exponentially as  $s$  decreases below  $1/2$ .

For the above reasons, the data for  $s = 0.2$  is clearly less accurate than for  $s \geq 0.3$ , as reflected by the error bars shown in Fig. 2c,d of the main text. The two extremal values that define the indicated error bars correspond to the two values of the exponent obtained by using only the upper or lower half of the full fitting interval that is indicated by vertical marks; the uncertainties from the straight power-law fit are somewhat smaller.

For  $s = 1/2$ , the transition is at its upper critical dimension and logarithmic corrections to the leading power laws are expected. As quantifying these corrections from the VMPS results is difficult, we have restricted ourselves to fits to effective power laws, which then naturally result in exponents slightly deviating from the mean-field values.

## C. Hyperscaling

For SBM1, a scaling ansatz for the singular part of the free energy can be used<sup>13</sup> to derive a hyperscaling relation between the critical exponents  $\delta$  and  $x$ , namely  $\delta = (1 + x)/(1 - x)$ . Here,  $x$  describes the divergence of the static susceptibility as  $T \rightarrow 0$  at criticality,  $\chi(T) \propto T^{-x}$  where  $\chi = \partial \langle \sigma_x \rangle / \partial h_x$ . Hyperscaling also implies  $x = y$ , where  $y$  characterizes the divergence of the zero-temperature dynamic susceptibility,  $\chi(\omega) \propto \omega^{-y}$ . Furthermore,  $y = s$  is an exact result for the critical long-range Ising chain at all  $s$  (Refs. 14,15). This finally yields

$$\delta = \frac{1 + s}{1 - s} \quad (\text{S30})$$

under the condition that hyperscaling is fulfilled, i.e., that no dangerously irrelevant operators spoils the naive scaling hypothesis. For the Ising chain, this applies below the upper critical dimension, i.e., for  $s > 1/2$ , while a dangerously irrelevant operator appears for  $s < 1/2$ . Consistent with the expectations from QCC, our  $\delta$ -values follow the hyperscaling prediction (S30) for  $s > 1/2$  (see Fig. 2d of main text).

## V. ADDITIONAL RESULTS FOR SBM2

### A. Determination of phase boundaries

Below we describe several approaches that we have found useful for determining the various phase boundaries of SBM2. For convenience, these boundaries are illustrated schematically in Fig. S10.

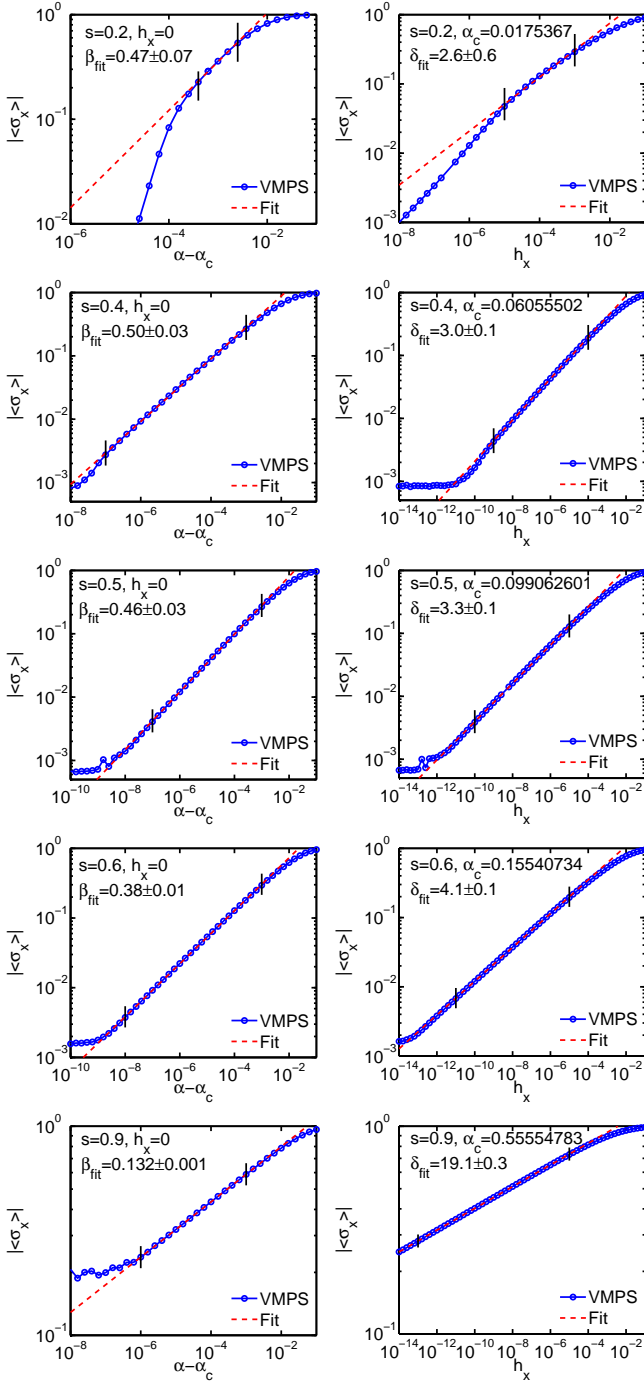


FIG. S9: The left and right columns show some of the VMPS results used to determine the SBM1 exponents  $\beta$  and  $\delta$  that are shown in Fig. 1c) and 1d) of the main text, respectively. We used  $h_z = 0.1$ ,  $\Lambda = 2$ ,  $L = 60$ ,  $D = 40$ ,  $d_{\text{opt}} = 12$ . The main text (Eq. (S29)) explains why the range of pure power-law behavior is smaller for  $s = 0.2$  than for larger  $s$ -values.

1. *Order parameter.* Measurements of the order parameter  $\langle \sigma_{x,y} \rangle$  of the localized phase can be used to determine the critical field  $h_z^c$  that defines the location of the L-D boundary at finite  $h_z$ . This is demonstrated in Fig. S11 for  $s = 0.6$  and  $\alpha = 0.1$ . The method of “best power laws” is then suitable to obtain accurate values for

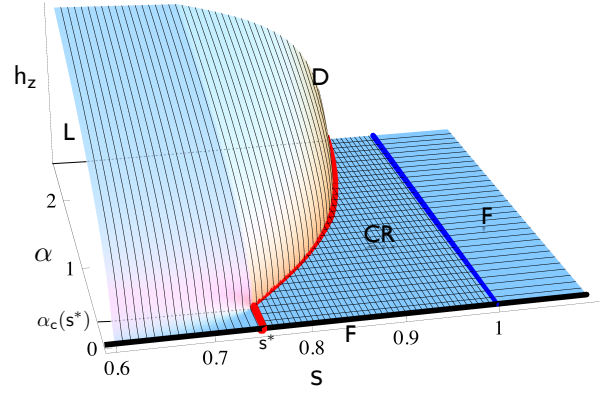


FIG. S10: Schematic sketch of the SBM2 phase diagram as function of  $s$ ,  $\alpha$  and  $h_z$ . The localized phase (L) lies below the curved surface representing the critical field  $h_z^c(s, \alpha)$ , the delocalized phase (D) above and to its right. (The curved surface was not calculated, but is an artist’s impression.) The cross-hatched area in the  $h_z = 0$  plane represents the critical phase (CR). Its phase boundary with the localized phase (L) is marked by the thick red line in the  $h_z = 0$  plane (corresponding to the red line in main text, Fig. 3a), consisting of a straight line between the points  $(s^*, 0)$  and  $(s^*, \alpha_c(s^*))$ , and a curved portion representing the line  $\alpha_c(s)$ , for  $s^* < s < 1$ . The thick blue line at  $s = 1$  is the CR-F phase boundary to the free phase (F). The thick black line at  $\alpha = h_z = 0$  likewise represents a free spin (F).

$h_z^c$  as well as corresponding critical exponents – we leave this for a future study.

Notably, the inherent instability of the CR phase, combined with numerical errors of VMPS, renders difficult the accurate determination of the CR-L phase boundary at  $\vec{h} = 0$ . In particular, a direct observation of the order parameter as function of  $\alpha$  or  $s$  leads to sizeable uncertainties.

2. *Transverse-field response.* The zero-field phase boundary CR-L is most accurately extracted via the response to a small transverse field,  $\langle \sigma_z \rangle(h_z)$ . The stable L phase responds linearly, while the CR phase responds with a non-trivial sublinear power-law, see Eq. (S32) below – those can be easily distinguished, as shown in Fig. 3b of the main paper. Indeed, by studying the transverse-field response for small  $\alpha$  and  $0.7 \leq s \leq 0.8$ , we are able to determine the value of the universal critical “dimension”  $s^*$  to be  $0.75 \pm 0.01$ , as shown in Fig. S12.

The accurate determination of  $s^*$  requires the numerical results to be reliable down to transverse fields as small as  $h_z \simeq 10^{-14}$ . Such precision is achievable, in principle, by using sufficiently large  $D$  and  $d_{\text{opt}}$ , as follows from Fig. S4. However, such a brute force approach is computationally demanding. A more efficient strategy is to exploit parity symmetry: For  $h_x = h_y = 0$  the SBM2 Hamiltonian commutes with the parity operator

$$\hat{P}_z \equiv \sigma_z e^{i\pi \hat{N}}, \quad (\text{S31})$$

where  $\hat{N} = \sum_k \hat{b}_{kx}^\dagger \hat{b}_{kx} + \sum_k \hat{b}_{ky}^\dagger \hat{b}_{ky}$  counts the total num-



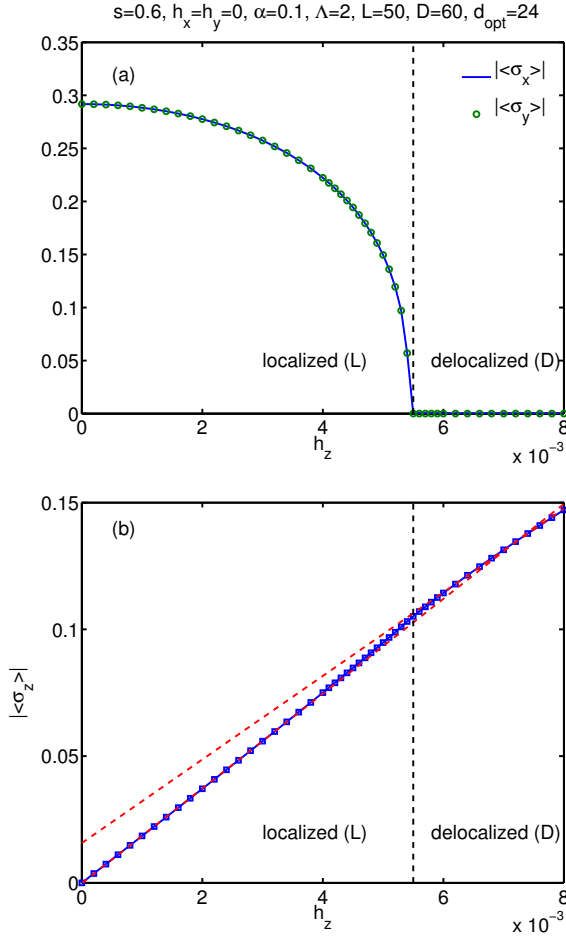


FIG. S11: (a) Order parameter  $|\langle\sigma_{x,y}\rangle|$  for the L-D transition, driven to zero by increasing the transverse field  $h_z$  past the critical value  $h_z^c$  (indicated by black dashed line). (b) Correspondingly, the transverse-field response of  $|\langle\sigma_z\rangle|$  shows a slight kink, indicating the higher-order singularity expected at the L-D transition. As in Fig. 3 of the main paper, the linear response of the L phase is clearly visible. We observe a small breaking of the XY symmetry of SBM2 in the L phase due to numerical errors, in that the order parameter in panel (a) prefers configurations with  $|\langle\sigma_x\rangle| = |\langle\sigma_y\rangle|$ , instead of exploring the full rotational symmetry.

ber of bosons on the entire Wilson chain. Thus, the ground state has a parity degeneracy. In fact, this degeneracy is the main source of numerical error for small  $h_z$  when using a VMPS code that does not account for parity symmetry, since then the degeneracy is lifted by numerical noise (similarly to the SBM1 case). By implementing this parity symmetry explicitly in the code, we were able to achieve the required precision (much better than in Fig. S4), while using choices for  $D$  and  $d_{\text{opt}}$  that were not unreasonably large, as shown in Fig. S12.

3. *Diverging boson number and flow diagram.* We have also explored alternative ways for determining the L-CR phase boundary, based on monitoring the divergence of the boson number per site at the end of the chain,

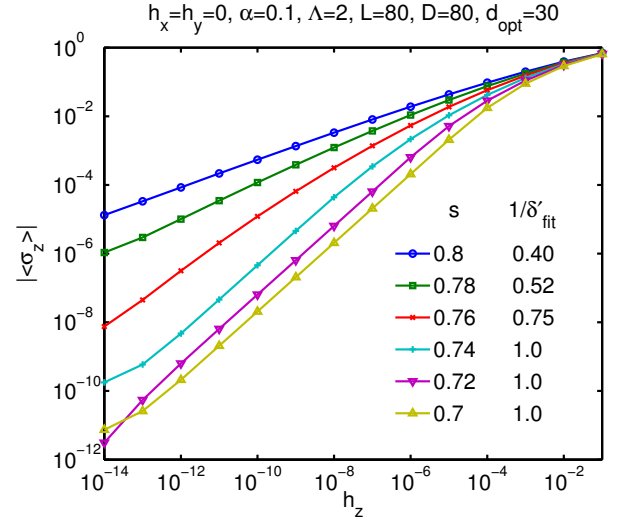


FIG. S12: Transverse-field response for SBM2,  $|\langle\sigma_z\rangle|$  vs.  $h_z$ , used to determine the L-CR phase boundary. The fitting exponent  $\delta'$  is defined in Eq. (S33), and the fitting range is  $h_z \in [10^{-12}, 10^{-8}]$ . From the transition between a linear response for  $s < s^*$  and a sublinear power law for  $s > s^*$ , we estimate  $s^*$  to lie between 0.74 and 0.76. To reduce numerical noise, the curves were calculated using a VMPS ground state that also was an odd eigenstate of the parity operator  $\hat{P}_z$  of Eq. (S31).

or analyzing NRG-like flow diagrams (as discussed for SBM1). We have found these methods to be computationally much cheaper than studying the transverse-field response, while yielding results of comparable accuracy for the L-CR phase boundary.

## B. Properties of the critical phase

The CR phase corresponds to a partially screened (or fractional) spin, with non-trivial power-law autocorrelations of the components of  $\vec{\sigma}$ . In ground-state calculations, those can be probed by measuring the response to an applied field: The linear-response susceptibility at  $T = 0$  is infinite, and the non-linear response is of power-law character,

$$\langle\sigma_{x,y}\rangle \propto h_{x,y}^{1/\delta}, \quad \langle\sigma_z\rangle \propto h_z^{1/\delta'}, \quad (\text{S32})$$

with  $\delta, \delta' > 1$ . A standard renormalized perturbation expansion around the free-spin fixed point results in<sup>17</sup>

$$\begin{aligned} 1/\delta &= \frac{1-s}{2} + \mathcal{O}([1-s]^2), \\ 1/\delta' &= 1-s + \mathcal{O}([1-s]^2). \end{aligned} \quad (\text{S33})$$

In Figs. S13 we show numerical VMPS data for the non-linear response for several sets of parameters inside the CR phase. We indeed find the expected power laws over a sizeable range of fields; the power laws are cut off at small fields by the influence of numerical errors, like

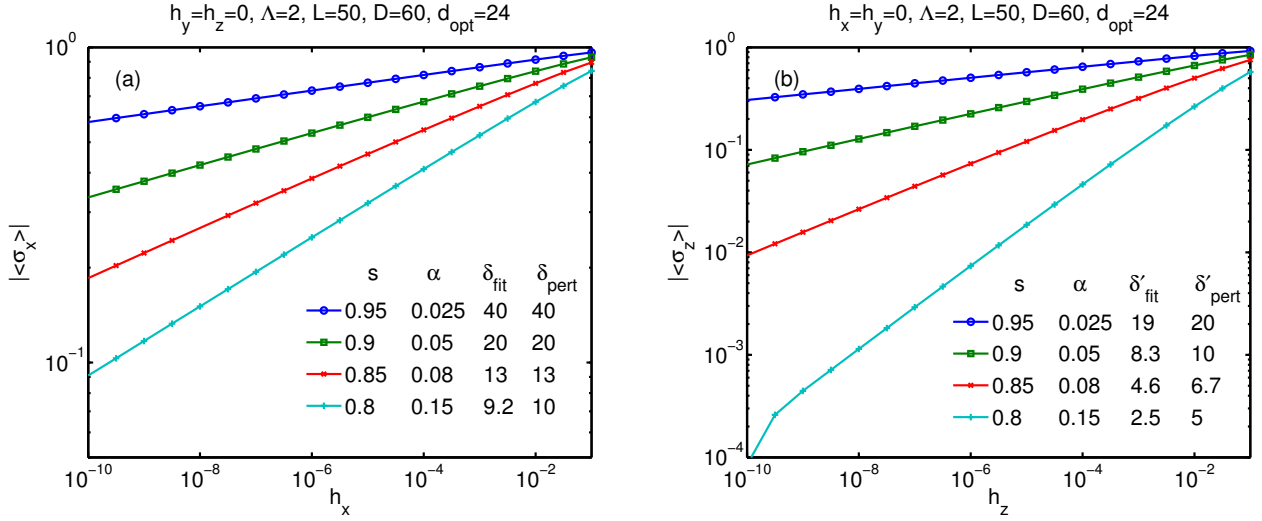


FIG. S13: Non-linear response *inside* the CR phase. We find power law behavior as expected from Eq. (S32). For each  $s$ , we chose an  $\alpha$ -value close to the  $\alpha^*$  fixed-point value, to ensure that the asymptotic power law is reached quickly (i.e. without the need for  $h_x$  to become extremely small). Using the fitting range between  $10^{-9}$  and  $10^{-2}$ , we find values for the exponents  $\delta_{\text{fit}}$  and  $\delta'_{\text{fit}}$  in excellent agreement with the values  $\delta_{\text{pert}}$  and  $\delta'_{\text{pert}}$  expected from Eq. (S33), as indicated in the legends.

the breaking of the XY symmetry of the model or the generation of a small transverse field. From the data we can extract exponents  $\delta$  and  $\delta'$  as function of  $s$ . Comparing the resulting exponents to the perturbative prediction (S33), we find that the agreement is excellent, considering that (i) for  $s$  very close to unity the asymptotic regime is difficult to reach, due to the slow flow of  $\alpha$ , and (ii) for larger  $(1-s)$  the second-order terms in Eq. (S33) (i.e. two-loop corrections) will become important.

### C. RG flow near $s^*$

Fig. 4 of the main text shows the RG flow of SBM2 in the two cases (a)  $s^* < s < 1$  and (b)  $0 < s < s^*$ . In case (a) the CR phase is stable for small  $\alpha$  and  $\vec{h} = 0$ , whereas this phase is absent in case (b). In the following we briefly discuss the evolution of the RG flow from case (a) to case (b), as this is related to a *discontinuous* jump of the phase boundary upon varying  $s$ .

As described in the main text, the fixed points CR and QC1 of case (a) approach each other upon lowering  $s$ , such that they meet at  $s = s^*$  and both disappear for  $s < s^*$ . This follows from the absence of the CR phase in case (b) and the fact that both are intermediate-coupling

fixed points for  $s < 1$  (i.e. they have to meet at finite  $\alpha$ ). The merger of the two fixed points also implies that the flow lines to the left and right of CR in Fig. 4a merge. As a result, the RG flow line which lead from F via CR to D in case (a) now becomes a flow line from F to QC2 in case (b). For the phase boundary of the L phase (thick line in Fig. 4) this means that its starting point on the  $h_z = 0$  axis jumps from a finite value (corresponding to QC1) in (a) to zero in (b) once  $s$  is lowered past  $s^*$ .

We note that the merger and disappearance of two fixed points upon variation of a “dimension”  $d$  is not unusual. For instance, upon approaching the lower critical dimension  $d_c^-$  of a magnet from above, the critical fixed point typically approaches the trivial fixed point describing the ordered phase, such that both merge at  $d = d_c^-$  and disappear for  $d < d_c^-$ . Here the evolution of the phase boundary is continuous. What is unusual about SBM2 is that two *intermediate-coupling* fixed points merge and disappear, causing the discontinuous behavior. The only other example with similar physics we are aware of is in the two-channel Anderson/Kondo impurity model with power-law density of states  $\propto |\omega|^r$ , where a critical fixed point merges with a stable non-Fermi liquid fixed point at some critical dimension  $r_{\text{max}}$ , with a consequent jump in the phase diagram.<sup>18,19</sup>

<sup>1</sup> K. G. Wilson, Rev. Mod. Phys. **47**, 773 (1975); R. Bulla, T. Costi, and T. Pruschke, Rev. Mod. Phys. **80**, 395 (2008).

<sup>2</sup> R. Bulla, N. Tong, and M. Vojta, Phys. Rev. Lett. **91**, 170601 (2003).

<sup>3</sup> R. Bulla, H. Lee, N. Tong, and M. Vojta, Phys. Rev. B **71**, 045122 (2005).

<sup>4</sup> C. Guo, A. Weichselbaum, J. von Delft, and M. Vojta, to be published.

<sup>5</sup> R. Žitko and T. Pruschke, Phys. Rev. B **79**, 085106 (2009).

<sup>6</sup> L. N. Oliveira, Braz. J. Phys. **22**, 155 (1992).

<sup>7</sup> S. R. White, Phys. Rev. Lett. **69**, 2863 (1992).

<sup>8</sup> C. Zhang, E. Jeckelmann, and S. R. White, Phys. Rev.

- Lett. **80**, 2661 (1998).
- <sup>9</sup> A. Weiße *et al.*, Phys. Rev. B **62**, R747 (2000).
- <sup>10</sup> Y. Nishiyama, Eur. Phys. J. B **12**, 547 (1999).
- <sup>11</sup> A. Alvermann and H. Fehske, Phys. Rev. Lett. **102**, 150601 (2009).
- <sup>12</sup> H. Saberi, A. Weichselbaum, and J. von Delft, Phys. Rev. B **78**, 035124 (2008).
- <sup>13</sup> M. Vojta, N. Tong, and R. Bulla, Phys. Rev. Lett. **94**, 070604 (2005).
- <sup>14</sup> M. E. Fisher, S. K. Ma, and B. G. Nickel, Phys. Rev. Lett. **29**, 917 (1972).
- <sup>15</sup> M. Suzuki, Prog. Theor. Phys. **49**, 424 (1973); **49**, 1106 (1973); **49**, 1440 (1973).
- <sup>16</sup> M. Vojta, arXiv:1201.4922 (2012).
- <sup>17</sup> L. Zhu and Q. Si, Phys. Rev. B **66**, 024426 (2002); G. Zarand and E. Demler, Phys. Rev. B **66**, 024427 (2002).
- <sup>18</sup> C. Buxton and K. Ingersent, Phys. Rev. B **57**, 14254 (1998).
- <sup>19</sup> I. Schneider, L. Fritz, F. B. Anders, A. Benlagra, and M. Vojta, Phys. Rev. B **84**, 125139 (2011).